

pubs.acs.org/JACS Article

Untangling the Interactions between Anionic Polystyrene Nanoparticles and Lipid Membranes Using Laurdan Fluorescence Spectroscopy and Molecular Simulations

Laura A. Kesner, Zeke A. Piskulich, Qiang Cui,* and Zeev Rosenzweig*



Cite This: https://doi.org/10.1021/jacs.2c13403



Read Online

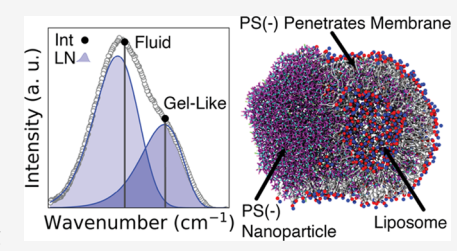
ACCESS I

Metrics & More

Article Recommendations

Supporting Information

ABSTRACT: Several classes of synthetic nanoparticles (NPs) induce rearrangements of cell membranes that can affect membrane function. This paper describes the investigation of the interactions between polystyrene nanoparticles and liposomes, which serve as model cell membranes, using a combination of laurdan fluorescence spectroscopy and coarse-grained molecular dynamics (MD) simulations. The relative intensities of the gel-like and fluid fluorescent peaks of laurdan, which is embedded in the liposome membranes, are quantified from the areas of deconvoluted lognormal laurdan fluorescence peaks. This provides significant advantages in understanding polymer—membrane interactions. Our study reveals that anionic polystyrene NPs,



which are not cross-linked, induce significant membrane rearrangement compared to other cationic or anionic NPs. Coarse-grained MD simulations demonstrate that polymer chains from the anionic polystyrene NP penetrate the liposome membrane. The inner leaflet remains intact throughout this process, though both leaflets show a decrease in lipid packing that is indicative of significant local rearrangement of the liposome membrane. These results are attributed to the formation of a hybrid gel made up of a combination of polystyrene (PS) and lipids that forces water molecules away from laurdan. Our study concludes that a combination of negative surface charge to interact electrostatically with positive charges on the membrane, a hydrophobic core to provide a thermodynamic preference for membrane association, and the ability to extend non-cross linked polymer chains into the liposome membrane are necessary for NPs to cause a significant rearrangement in the liposomes.

■ INTRODUCTION

The potential for adverse impacts of engineered nanoparticles (NPs) on organisms and the environment has become an increasing area of concern due to the large increase in production of NPs and their prevalence in society. 1-4 Consequently, there is an impetus to design more benign NPs. Numerous studies of the interactions of synthetic NPs with cell membranes have revealed that such interactions could have significant impacts on the health of the exposed organism. 1-5 NPs are known to interact with cellular membranes via a variety of mechanisms, including membrane association or disruption, membranal morphological changes, NP wrapping/uptake, reactive oxygen species (ROS) generation, NP ion dissolution, and lipid corona formation around the NP. 1-6 Previous studies of the interactions between NPs and membranes predominantly focused on acute interactions, which cause severe membrane disruption. Disruptive interactions primarily involve NPs with cation-terminated aliphatic ligands; anionic NPs have been largely ignored due to the lack of disruptive interactions. Chronic NP exposures can lead to adaptation by cells⁷ and organisms,⁸ which implies that some interactions induce toxic effects without destroying membranes or killing cells.

The rearrangement of lipids in the membrane when interacting with anionic NPs has been previously demonstrated

to lead to membrane destruction. 3,9,10 The lipid phase of a cellular membrane is an important characteristic that affects signaling and molecular mobility, and it is used as a metric of membrane health and response to stimuli. 11-13 Tightly packed lipids form a rigid phase called the solid-ordered (gel) phase, in which the lipids diffuse slowly, and few water molecules intercalate while loosely packed lipids form a liquid-disordered (fluid) phase, in which water molecules diffuse more easily and in greater number. 11,14 Fluorescence spectroscopy is a sensitive and nondestructive method commonly used to measure membrane phase changes. Fluorophores like dimethylaminonaphthalene (DAN) derivatives, particularly laurdan (6dodecanoyl-2-dimethylamine-naphthalene), partition into lipid membranes and are used as probes of the membrane phase.¹⁵ When dissolved in organic solvents and excited with UV light, the emission maximum of laurdan shifts from 403 to 506 nm as solvent polarity increases from cyclohexane to methanol, independent of temperature. 15,16 When incorpo-

Received: December 16, 2022



rated into lipid membranes, laurdan exhibits two emission peaks at $440 \text{ nm} (22,727 \text{ cm}^{-1})$, which is attributed to the gel phase, and at 490 nm (20,408 cm⁻¹), which is attributed to the fluid phase of the membrane. This red shift in the fluorescent signal in the membrane fluid phase originates from laurdan interactions with water molecules which are better able to access the membrane due to the looser lipid packing and their ability to reorganize and stabilize the probe's excited state. Laurdan fluorescence spectroscopy has long been used to measure phase changes in unilamellar phospholipid vesicles (liposomes) exposed to various stimuli, with the understanding that it is an indirect measure of lipid phase or packing through a quantification of the water around the fluorophore. Liposomes are commonly used to model cellular membrane due to their relative simplicity, which enables precise control of their composition and structure. Thus, liposomes provide an ideal medium for the quantitative determination and comparison of NP-membrane interactions.

A generalized polarization (GP) parameter, which was first introduced by Parasassi et al., is commonly used to quantify the membrane phase. ¹⁹ GP is calculated using the following equation:

$$GP = \frac{I_{440} - I_{490}}{I_{440} + I_{490}} \tag{1}$$

where I_{440} and I_{490} are the laurdan fluorescence intensities at 440 nm (gel) and 490 nm (fluid), respectively; GP approaches 1 as the lipid phase becomes more gelled, and it approaches -1 as it becomes more fluid. In the use of laurdan fluorescence to measure nanoparticle-induced membrane gelation, the greatest concern is the mole fraction of the membrane with gel-like lipids $(X_{\rm gel})$, which is calculated as follows:

$$X_{\text{gel}} = \frac{n_{\text{gel}}}{n_{\text{total}}} = \frac{I_{\text{gel}}}{I_{\text{gel}} + I_{\text{fluid}}}$$
(2)

where $n_{\rm gel}$ is the number of gel-like laurdan molecules present, $n_{\rm total}$ is the total number of laurdan molecules, $I_{\rm gel}$ is the fluorescence intensity (or area) due to the gel-like phase, and $I_{\rm fluid}$ is the fluorescence intensity (or area) due to the fluid-like phase. Here, we use the phrases "gel-like" and "fluid-like" to describe this change for clarity, as traditional interpretation of laurdan is complicated when a hydrophobic species dissolves into the hydrophobic region, as will be demonstrated in the present work.

Although GP is a quick and popular quantification of membrane phase using laurdan, spectral overlap of the two peaks limits the range of achievable values much narrower than the theoretical -1 to +1 and convolutes the results. 16 Methods proposed to address this include deconvolution into two Gaussians²⁰ or two lognormal functions (mirror symmetric form). 16 Both cases first convert the spectral domain to the wavenumber $(\tilde{\nu})$ domain and correct the intensity using the eq $I_v = I_{\lambda} \lambda^2$ (where I_v is the intensity in the wavenumber domain, I_{λ} is the intensity in the wavelength domain, and λ is the wavelength omitting the units) to account for the change in intensity distribution resulting from this conversion. 16,20 The areas of these peaks are then used in place of the intensities in the GP or other equations. A major challenge with deconvolution is arbitrarily selecting a function such as a Gaussian, which may yield a greater number of component peaks than there are electronic transitions.²¹ The shape of the component peaks must therefore be well-characterized.²¹

Many organic molecules do not exhibit symmetrical absorbance or emission peaks due to a skew caused by a difference in the distribution of vibrational energy levels between the ground and excited states. 16 The lognormal function fits these skewed absorptions, 21 and the mirror symmetric form fits the emission spectra ($R^2 > 0.997$ for all solvents tested).²² Liposomes of 1,2-dimyristoyl-sn-glycero-3phosphocholine (DMPC) labeled with laurdan exhibit a stronger change in the relative area of the deconvoluted peaks as temperature increases from 5 to 55 °C than if the same spectra were quantified using peak intensities alone or deconvolution into Gaussians. 16 The plot of each peak's intensity vs temperature is sigmoidal rather than stepwise, and the extremes still have vestiges of the non-dominant peak (e.g., a small gel-like peak well above the phase transition temperature); however, the ratio of the areas of the two peaks is linear for a 20 °C span of temperatures of DMPC, beginning just below the phase transition.¹⁶ This indicates a gradual change in hydration (and therefore lipid packing) even beyond the phase transition. In our study, we have used the lognormal function to quantify the fluorescence peaks of laurdan in labeled membranes exposed to nanoparticles. A detailed description of the calculation of the lognormal function is provided in the Supporting Information document.

Fluorescence spectroscopy of laurdan-labeled liposomes was previously used to investigate the impact of NPs on the membrane structure. Wei et al. exposed positively charged and negatively charged liposomes to various oxide NPs and determined that negatively charged zinc oxide and positively charged aluminum oxide induce gelation of liposomes with opposite charges but not those with the same charge as the NPs.³ The more negatively charged silica induces strong gelation of positive liposomes and mild gelation of negative liposomes. The change in FT-IR absorption of C=O bonds and phosphate groups in the lipids, which are gelled due to the NPs, suggests that hydrogen bonding plays a role in the interactions inducing gelation. Kanwa et al. found that negatively charged gold NPs with different functional groups (mercaptopropionic acid, citrate, and glutathione) all cause gelation of PC and inverted PC liposomes. 10 Steric hindrance of the anionic functional group distances the NP from the membrane, decreasing this effect, and cationic cysteaminefunctionalized gold NPs cause minimal gelation of PC liposomes. 10 Wang et al. found that positively charged polystyrene (PS) NPs slightly increase PC liposome fluidity, while negatively charged PS NPs cause significant liposome shrinkage in size of up to 20% which was interpreted as a transition of the lipids to the gel phase. The authors proposed that the mechanism of interaction is a change in the head group tilt angle causing a change in packing density of the lipids. As we will demonstrate below, our combined experimental and theoretical results indicate that the mechanism of interaction between PS NPs and lipid membranes may be more complicated than has previously been considered.

In the present study, we have exposed laurdan-labeled liposomes to varying concentrations of PS(-) NPs and demonstrate the efficacy of the lognormal approach to obtaining $X_{\rm gel}$ by comparing it with the typical GP approach. In tandem, we have employed coarse-grained molecular dynamics (MD) simulations to gain molecular-level insight into the interactions between PS(-) NPs and lipid membranes. Our study reveals a more nuanced mechanism

of the interactions between PS NPs and lipid membranes than previously reported. It shows that PS NPs without cross-links can penetrate the hydrophobic region of the lipid membrane. Our results are best described by a gel-like hybrid being formed by the combination of PS chains and lipids that forces water out of the membrane, leading to a gel-like signal from laurdan.

MATERIALS AND METHODS

Experimental Studies. Reagents. Laurdan was obtained from Thermo Fisher Scientific. Methanol was obtained from Fisher $Scientific. \ 1-Palmitoyl-2-oleoyl-glycero-3-phosphocholine \ (POPC,\ 25$ mg/mL in chloroform) was obtained from Avanti Polar Lipids. Phosphate-buffered saline (PBS) packets (final solution 10 mM phosphate, 15 mM NaCl, pH 7.2) were obtained from Thermo Scientific. 4-(2-Hydroxyethyl)-1-piperazineethanesulfonic acid (HEPES) (1 M, pH 7.4 stock solution) was obtained from Fisher Scientific. An extruder kit and polycarbonate membrane filters were obtained from Avanti Polar Lipids. Carboxylated polystyrene nanoparticles (PS(-) NPs) (40 nm diameter, 10% w/v solution) and aminated polystyrene nanoparticles (PS(+) NPs (50 nm diameter, 10% w/v solution) were purchased from MagSphere Inc. In this study, we tested our lognormal approach using a variety of other nanoparticles. These included succinylated phytoglycogen nanoparticle powder (PhG) (ca. 60 nm diameter hydrated) that was obtained from Mirexus Biotechnologies Inc. and carboxylated detonation nanodiamond nanoparticles (ND) that were purchased from Adámas Nanotechnologies (30 nm diameter, 1% w/w suspension in deionized water), and collaborators at the Hamers laboratory (University of Wisconsin-Madison) provided us lithium cobalt oxide (LCO, <100 nm)²³ and nickel manganese cobalt (NMC, ~100 nm diameter, 5 nm thick) nanosheet powders.²

Liposome Preparation. Liposomes were prepared using a dry film rehydration method.²⁵ Laurdan was dissolved in methanol at a concentration of 0.1 mg/mL. POPC and the previously prepared laurdan in methanol were combined in a 100/0.1 mol lipid/mol laurdan ratio in a scintillation vial for each batch. The vials were swirled under a stream of nitrogen until a dry film formed. The films were further dried under vacuum overnight to remove any remaining solvent. The films were rehydrated with 10 mM PBS or HEPES buffer (for use with NPs unstable in phosphate) at pH 7.2 to produce a lipid concentration of 2 mM. The vials were swirled in a dry ice/acetone bath $(-78 \, ^{\circ}\text{C})$ until the solution froze, and then they were thawed in a room-temperature bath sonicator. This freeze/thaw cycle was repeated for a total of 10 times to produce unilamellar liposomes. Immediately before use, liposome solutions were extruded through a mini extruder with a 400 nm polycarbonate membrane 11 times and then a 200 nm membrane 11 times.

Fluorescence Spectroscopy. Liposomes were diluted to approximately 0.5 nM with PBS by diluting 96 μ L aliquots of prepared liposomes to 1 mL. Fluorescence steady-state emission spectra from 380 to 620 nm were acquired on a PTI-Horiba QuantaMaster 400 fluorimeter using 356 nm excitation, 2 nm slits, 0.3 s integration, 1 nm step size, and excitation gain such that the output is approximately 1.3 V (the signal is to be kept between 1 and 2 V to optimize the signal-to-noise ratio and linearity of instrument response). Sample temperature was kept at 20 °C. All fluorescence spectra were corrected for instrument response by the Felix GX acquisition software.

Dynamic Light Scattering (DLS) and Zeta (ζ) Potential Measurements. DLS and ζ potential measurements were performed on liposomes (diluted 10 μ L of liposome stock to 1 mL) and NPs in disposable cuvettes at 25 °C using a Malvern ZetaSizer Nano ZS. The settings used for the liposomes were refractive index 1.45, absorption 0.001, and measurement angle of 173°. Refraction index and absorbance were adjusted for each NP core. ζ potential measurements were made using a dip cell with monomodal analysis to minimize sample degradation. DLS and ζ potential for both the liposomes and

the NPs are reported in Figures S1 and S2 in the Supporting Information.

Nanoparticle Exposures. PBS was chosen as the buffer for all NP exposures and measurements in this paper whenever possible due to its similar osmolarity to biological systems. ND, NMC, and LCO were solubilized in HEPES buffer at pH 7.2. POPC liposomes were prepared in PBS as described above. PS(-) and PS(+) NPs were washed in a centrifuge (10,000×g for 10 min) and resuspended in PBS immediately before use to remove the surfactant. PhG was solubilized in PBS immediately before use. UV-visible absorbance was performed on an Agilent Cary 3500 UV-Vis spectrophotometer. Liposomes (approximately 0.5 nM) and NPs (0, 5, 10, or 25 nM PS(-) and PhG NPs or 0, 1, 5, or 25 mg/L LCO or NMC were suspended in buffer-containing microcentrifuge tubes (the same one each NP was solubilized in) and mixed on a rocking platform shaker at room temperature for 3 h. Experiments were done in quadruplicate. All fluorescence spectra were converted to the wavenumber domain and the intensity adjusted with the equation $I_v = I_2 \lambda^2$. Fluorescence blanks of NPs and PBS were subtracted from sample fluorescence (after wavenumber correction) to remove scattering from NPs and Raman scattering from water. The scattering from liposomes was subtracted based on deconvolution as described below. No control could be made for the effect of the NPs on the laurdan itself because laurdan, as a lipid analogue, is not itself soluble in water without forming a micelle, vesicle, or other structure with other laurdan molecules to minimize interactions between the water and the hydrophobic tails, and the 0.1% concentration of laurdan in the liposomes should prevent laurdan molecules from neighboring each other.

Membrane Phase Determination. Lognormal Deconvolution. Blank-subtracted spectra were fitted to two Gaussians (for the liposome scattering) and two LN functions using a Python code (see Supporting Information). The integrated areas of the gel and fluid LN peaks were used for $I_{\rm gel}$ and $I_{\rm fluid}$ to calculate the gelation fraction using the lognormal deconvolution ($X_{\rm gel}$ LN). The fitted scattering Gaussians were subtracted from the blank-subtracted spectra, and these scatter-subtracted spectra were used for the remaining Gaussian fitting and intensity calculation.

Gaussian Deconvolution and Intensity Calculation. Scatter-subtracted spectra were deconvoluted into two Gaussians using a Python code (see Supporting Information). The integrated areas of the fluid and gel Gaussian peaks were used for $I_{\rm gel}$ and $I_{\rm fluid}$ to calculate the gelation fraction in using the Gaussian deconvolution ($X_{\rm gel}$ Gauss); (c) Fluorescence peak intensity: Fluorescence intensities of the scatter-subtracted spectra at 490 and 440 nm (20,408 and 22,727 cm⁻¹) were used for $I_{\rm gel}$ and $I_{\rm fluid}$ to calculate the gelation fraction using the intensity calculation ($X_{\rm gel}$ Int).

Statistical Analysis. The mean $X_{\rm gel}$ values for each concentration within each calculation method (Int and LN) were compared using a one-tailed analysis of variance (ANOVA) test and Tukey's Honest Significant Difference Test. The limit of detection (LOD) and 95% confidence intervals of the LOD of NP-induced membrane structural change of each calculation method were quantified based on the method developed by Holstein et al. using the four-parameter logistical curve (4PL) commonly used in bioassays of binding events. The method is summarized in Figure S4. The LODs were compared using Welch's t-test.

Computational Studies. Coarse-Grained Force Fields. For the simulations, the coarse-grained MARTINI 2.2 model was used to describe molecular interactions of all species.²⁷ For polystyrene, the model developed by Rossi and co-workers was modified to include a P4 or Qa bead attached to the polymer backbone to represent the protonated and unprotonated state of the carboxyl group, respectively.²⁸ The MARTINI bead mapping scheme for PS is shown in Figure S7. The availability of the polymer force field in version 2.2 of the MARTINI force field was the rationale for not using the newest version (3.0) of the MARTINI model. For all simulations, 10% of water beads were randomly replaced with MARTINI antifreeze beads.

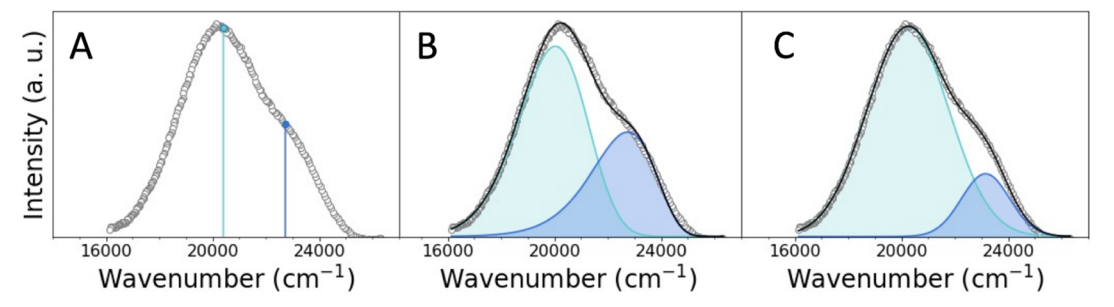


Figure 1. Quantification of $X_{\rm gel}$ from the scatter-subtracted spectra of POPC liposomes using three different methods: (A) intensity (Int), (B) lognormal deconvolution (LN), and (C) Gaussian deconvolution (Gauss). Aqua lines and shaded regions represent quantification of the fluid phase, and dark blue lines and shaded regions represent quantification of the gel-like phase.

Preparation of Simulated Liposomes. Initial positions for a coarse-grained POPC liposome were generated using the Chemistry at HARvard Macromolecular Mechanics Graphical User Interface (CHARMM-GUI).^{29–31} The generated system included 923 POPC lipids, 98,051 water beads, and 1083 Na+ and 1083 Cl- beads. A similar system with DOPC lipids was prepared in the same way as described within this section and was also built (containing 891 lipids, 97,682 water beads, and 1079 ion pairs) and analyzed in the same manner as described for POPC in this paper, the results for which is included in the Supporting Information. Simulations were run with the Large-Scale Atomic/Molecular Massively Parallel Simulator (LAMMPS) software package.³² Three cylinders were added along the x, y, and z axes with a radius of 2 nm. These cylinders were set to only allow the passage of water and ion beads through them to facilitate equilibration of the internal pressure of the liposome. Initial coordinates were minimized with an energy tolerance of 1.0×10^{-5} and a force tolerance of 1.0×10^{-7} . Initial velocities were then selected from the Maxwell-Boltzmann distribution at 300.0 K. With a simulation timestep of 10.0 fs, 100 steps were run in the microcanonical (NVE) ensemble to further relax the initial structure. The ensemble was then switched to the isobaric-isothermal (NpT) ensemble set to a reference pressure of 1.0 atmosphere.³³ The Nosé— Hoover thermostat and barostat damping parameters were set to 2000.0 and 20,000.0 fs, respectively. 34,35 Both the thermostat and barostat utilized a Nosé-Hoover chain length of 3. Simulations in this ensemble were then run for 15 ns. The timestep was subsequently increased to 20 fs, and simulations were run for a further 200 ns. The cylinders were removed, and a further 20 ns of simulation were run for further equilibration. Following this, a long equilibration simulation with the same parameters was run for 1.1 μ s.

Preparation of the Simulated Polymer. An approximately 6 nm polystyrene particle was built as a single chain without cross-links with 5000 regular polystyrene beads and 600 carboxylated polystyrene beads. The number of carboxylated groups was selected based on the 'parking area" of $80.6 A^2/\text{COOH}$ provided by the manufacturer of the PS beads used in the experimental studies. Of these, slightly under a third partitioned into the interior of the PS particle, leading to a final parking area of $\sim 112 \text{ Å}^2/\text{COOH}$, thus slightly less dense than experiment. A random sequence of these beads was input into the genpoly program included with the Moltemplate package in order to build a randomized self-avoiding polymer configuration.³⁶ To this, 62,899 water beads, 5307 Na⁺ beads, and 5307 Cl⁻ beads were added. Three variations of this system in total were generated, the first of which had all 600 carboxyls fully protonated. The second variation replaced half of these carboxyls with unprotonated beads (hereafter referred to as half-protonated) and 300 of the water beads were converted to Na+ beads to preserve charge neutrality. The final variation converted the remaining 300 protonated carboxyls to unprotonated (hereafter unprotonated) and again converted another 300 water beads to Na+ beads. Energies were minimized using the same procedure described above. A simulation was then run in the NpT ensemble with a timestep of 1.0 fs at 300 K and 1 atm for 50 ps. For the entire equilibration run, the thermostat and barostat damping parameters were set to be equal to 10*dt and 100*dt, respectively,

where dt is the timestep. A further 1 ns was then run with a 10.0 fs timestep. We then increased the timestep to 20.0 fs and pursued an annealing-like simulation scheme in the canonical (NVT) ensemble where we increased the temperature from 300 to 600 K uniformly over a period of 20 ns, held it at 600 K for 20 ns, and then uniformly decreased the temperature back down to 300 K for 20 ns. This was done to sample polymer configurations more quickly. The ensemble was switched back to the NpT ensemble, and simulations were run for 4 ns for final equilibration.

Preparation of the Combined System. Fully equilibrated configurations of the polystyrene and liposome simulation cells were shifted using Visual MD (VMD) such that the polystyrene began on the far-right edge of the simulation cell and the liposome began on the far-left. Simulations were then again energy minimized to remove bad overlaps (tolerances 1×10^{-4} and 1×10^{-6} for energy and forces, respectively).³⁷ A short 10 ps trajectory with a 1.0 fs timestep was then run in the NVE ensemble to bring the two simulation cells fully into contact. A simulation in the NpT ensemble was then run for $10\,$ ps before increasing the timestep to 10.0 fs and being equilibrated for 20 ns. The timestep was increased again to 20.0 fs and then run for 1.2 μ s in the NpT ensemble.

Area per Lipid Calculations. For simulations of PS interacting with liposomes, calculation of area per lipid in the usual way with spherical Voronoi analysis is challenging due to the asphericity induced in the liposome by PS. In the present work, we have implemented a similar approach for calculating area per lipid as is used by the FATSLiM software, which we will briefly detail.³⁸ This approach first identifies the leaflets of all lipids using the MDAnalysis LeafletFinder module.³⁵ For a particular leaflet, we then find the nearest neighbors within a 1.5 nm radius of each lipid. Singular value decomposition is then used to obtain an approximate plane shared by these lipids, as well as the vector normal to this plane. Lipid head group coordinates are then projected orthogonally onto this plane, and coordinates are converted into 2D planar coordinates. Voronoi analysis in this plane is then used to find the area of the central lipid.

RESULTS AND DISCUSSION

In this section, we first demonstrate the efficacy of the lognormal approach for deconvoluting laurdan fluorescence spectra and then demonstrate using this approach to show that PS(-) NPs induce changes to laurdan fluorescence not observed for other types of NPs. Lastly, we demonstrate using MD simulations that these changes appear to originate from penetration of the membrane by polymer chains.

Characterization of Liposomes Using Lognormal **Decomposition.** To demonstrate the efficacy of the lognormal approach to obtaining X_{gel} , we first apply the approach to a pure POPC liposome. A representative scattersubtracted fluorescence spectrum of laurdan in POPC liposomes is shown in Figure 1 with representations of an intensity-based calculation (panel A), in which the intensities at 20,408 cm⁻¹ (490 nm) and 22,727 cm⁻¹ (440 nm) are used

for the fluid and gel-like intensities, respectively; lognormal deconvolution, in which the spectrum is deconvoluted into two LN functions for the fluid and gel-like peaks (panel B); and Gaussian deconvolution, in which the spectrum is deconvoluted into two Gaussian functions for the fluid and gel-like peaks (panel C). $X_{\rm gel}$ and R^2 values for this sample are summarized in Table 1. We find that for a pure POPC

Table 1. $X_{\rm gel}$ of POPC Liposomes and Average R-Squared of Fit from Three Different Quantification Methods

	$X_{ m gel}$ Int	X_{gel} LN	X_{gel} Gauss
$X_{ m gel}$	0.351 ± 0.001	0.345 ± 0.002	0.152 ± 0.003
average R ²	N/A	0.9982	0.9994

liposome, the LN approach appears to provide reasonably similar R^2 values while better capturing the proportion of gellike lipids. It should be noted that all three techniques find a small gel-like peak for a pure POPC membrane, which was unexpected as experiments were conducted at temperatures well above (nearly 30 K) the fluid/gel transition temperature. Our hypothesis is that the presence of laurdan makes minor changes to the structure of the local membrane surrounding it, leading to a small gel-like contribution in the fluorescence. Further study is needed to understand this phenomenon.

NP-induced gelation experiments involving a variety of NPs were analyzed for $X_{\rm gel}$ LN and $X_{\rm gel}$ Gauss, and both yielded similar trends but different absolute values (data not shown). A Gaussian deconvolution may appear to be a better fit of the spectrum than a lognormal deconvolution based on R^2 (Table 1), but it overly favors the fluid phase: the gel peak is significantly smaller than the fluid peak in Figure 1C, and the $X_{\rm gel}$ is significantly lower (0.152 \pm 1.73% $X_{\rm gel}$ Gauss vs 0.351 \pm 0.42% $X_{\rm gel}$ Int and 0.345 \pm 0.62% $X_{\rm gel}$ LN). This is because the sum of the two overlapping peaks causes the fluid peak to appear like a Gaussian around 21,000 cm⁻¹. Qualitatively, the

 $X_{\rm gel}$ Int and $X_{\rm gel}$ LN fits agree with MD simulations of POPC membranes: the $X_{\rm gel}$ Gauss fit does not fully account for changes in the area per lipid with increasing membrane fluidity at elevated temperatures. ⁴¹ If the fraction in the gel phase were 0.152 at 20 °C (293 K) as measured with the Gaussian deconvolution, the area per lipid would not significantly increase at temperatures above 20 °C. In addition, the Gaussian deconvolution produces peaks whose maxima drift more significantly than the LN deconvolution's peaks as the temperature increases, and at low temperatures in which the gel phase is expected, the area for the fluid Gaussian peak is significantly higher than that of the gel peak. ¹⁶ The greater weight given to the fluid phase in $X_{\rm gel}$ Gauss and the higher error suggest that $X_{\rm gel}$ Gauss is not a reliable quantification method.

As X_{gel} Int and X_{gel} LN are in close agreement, it is useful to briefly compare the analytical figures of merit for X_{gel} Int and $X_{\rm gel}$ LN. To do this, we have exposed POPC/0.1% laurdan liposomes to PS(-) in concentrations ranging from 0 to 25 nM and calculated $X_{\rm gel}$ Int and $X_{\rm gel}$ LN for all samples. Averages of the scatter-subtracted spectra are shown in Figure 2A. The peak for the gel-like phase ($\approx 23,000 \text{ cm}^{-1}$) clearly increases relative to the fluid peak (\approx 20,000 cm $^{-1}$) with increasing PS(-) concentration, which is consistent with previous studies. 9 X_{gel} Int and X_{gel} LN as functions of PS(-) concentration are shown in Figure 2B, with the lower concentrations expanded in the inset for clarity. The means for each method at each concentration were compared using Tukey's Honest Significant Difference Test in Python. 42 The p-values comparing the lowest concentrations within a method are summarized in Table 2, and the p-values comparing methods at each concentration are summarized in Table 3. All concentrations of 5 nM and above are statistically different. Bolded values represent statistical significance (α = 0.05). X_{gel} Int at [PS(-)] = 0 and 0.5 nM are not statistically different (p> 0.05), while X_{gel} LN at [PS(-)] = 0 and 0.5 nM are

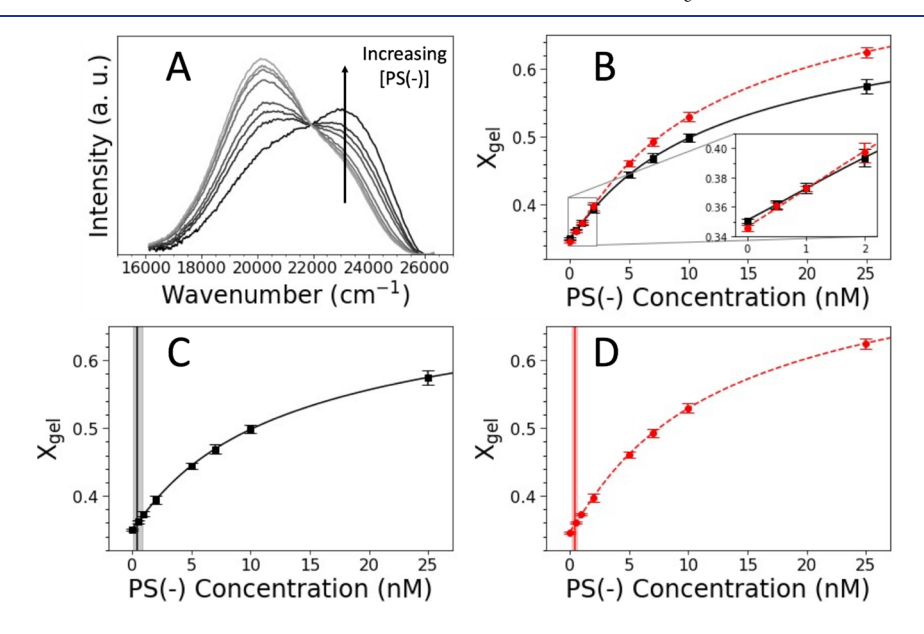


Figure 2. Comparison of fraction in the gel phase $(X_{\rm gel})$ calculated using intensities $(X_{\rm gel})$ and lognormal deconvolution $(X_{\rm gel})$ LN: (A) scatter-subtracted fluorescence spectra of laurdan in POPC liposomes exposed to varying concentrations of PS(-); (B) $X_{\rm gel}$ Int (black squares) and $X_{\rm gel}$ LN (red circles) as a function of PS(-) concentration with 4PL fitting curves (Int solid black, LN dashed red, inset is the 0–2 nM PS(-) region in greater detail); (C-D) $X_{\rm gel}$ as a function of PS(-) concentration fitted to a 4PL curve with LOD (vertical line) and 95% confidence interval of the LOD (vertical shaded region for (C) $X_{\rm gel}$ Int and (D) LN. Error bars represent one standard deviation.

Table 2. P-Values for Tukey's Honest Significant Difference Test between Concentrations for X_{gel} Int and X_{gel} LN (within Each Method)^a

concentrations (nM)	$X_{ m gel}$ Int	X_{gel} LN
0-0.5	0.2592	0.0186
0-1	<0.001	< 0.001
0-2	<0.001	<0.001
0.5 - 1	0.2093	0.1683
0.5-2	< 0.001	< 0.001

^aThe smallest possible value is <0.0001. Bolded values represent statistical significance.

Table 3. P-Values for Tukey's Honest Significant Difference Test between Methods for the Same Concentrations^a

concentration (nM)	Int to LN
0	0.9
0.5	0.9
1	0.9
2	0.9
5	0.0041
7	< 0.001
10	< 0.001
25	< 0.001

^aThe smallest possible value is <0.0001. Bolded values represent statistical significance.

statistically different (p=0.0186) (Table 2). Neither $X_{\rm gel}$ Int and $X_{\rm gel}$ LN are statistically different between [PS(-)]=0.5 and 1 nM (p>0.05), but all other comparisons are statistically different for both methods (p<0.001). This indicates that while both methods can quantify a difference in $X_{\rm gel}$ for higher concentrations of PS(-), only $X_{\rm gel}$ LN can detect a difference between 0 and 0.5 nM PS(-), which makes it advantageous over $X_{\rm gel}$ Int when quantifying small changes resulting from exposure to either small concentrations of NPs or to NPs which cause less membrane modifications than PS(-).

In comparing the methods at the same concentrations, the *p*values indicate statistical significance at 5 nM PS(-) (p < 0.01) and above (p < 0.001) (Table 3). X_{gel} LN reports a higher increase in gelation than $X_{\rm gel}$ Int due to the overlapping peaks, and so, the intensities at 20,408 and 22,727 cm⁻¹ are the sums of two separate peaks at those wavenumbers. Indeed, the maximum of the lognormal fluid peak is lower than the height achieved by the intensity method, and the low-energy tail of the lognormal gel-like peak contributes to the overall maximum at 20,408 cm⁻¹, as seen in Figure 2. The breadth of these peaks is due to variations in the vibrational and rotational energy levels for the same electronic transition, 43 so the peak area is a more accurate quantification of the number of molecules fluorescing than the intensity at one wavenumber, which ignores this broadening. As seen in temperatures well above or below the lipid $T_{\rm m}$, in which only one membrane phase is expected to be found, the shape of each peak is closer to that of a lognormal function. ¹⁶ Following the common assumption of a two-state system consisting of a relaxed fluid state and non-relaxed gel-like state, 16 the shapes of the peaks would not change as the phase changes with temperature or external stimulus but only the intensities of those peaks. It is therefore reasonable to assume that the peaks retain the shape of a lognormal function even in phase mixtures. Furthermore, as discussed in the ESI, analysis of the detection limit suggests

that the lognormal approach provides greater certainty when distinguishing between different lipid phases. In the following section, we use this approach to demonstrate that anionic polystyrene particles produce a unique modulation of the membrane structure.

Effect of Nanoparticle Identity and Charge on Laurdan Fluorescence. Most cell membranes possess a negative charge due to charged headgroups such as phosphatidylinositol and phosphatidylserine in animal cells and phosphatidylglycerol in bacterial cells. 44 Positively charged NPs and negatively charged NPs are known to interact differently with negatively charged lipid bilayers: cationic NPs induce lysis in negatively charged membranes; 5,6,45,46 while anionic NPs adsorb on the surface or embed within the bilayer 47 form lattice aggregates within the bilayer 48 or, in the case of anionic dendrimer-coated NPs, cause surface disruptions capable of inducing leakage. 49 This portion of the experiment sought to determine if there is a difference in effect of cationic vs anionic NPs on the laurdan fluorescence.

Averaged scatter-subtracted fluorescence spectra of laurdan in POPC liposomes exposed to varying concentrations of PS(-) and PS(+) NPs are shown in Figure 3A,B. The gel-like peak slightly increases relative to the fluid peak from exposure to PS(+) NPs (Figure 3B) but significantly less than the increase from PS(-) NPs. X_{gel} is plotted as a function of PS NPs' concentration in Figure 3C for both NPs. The increase in

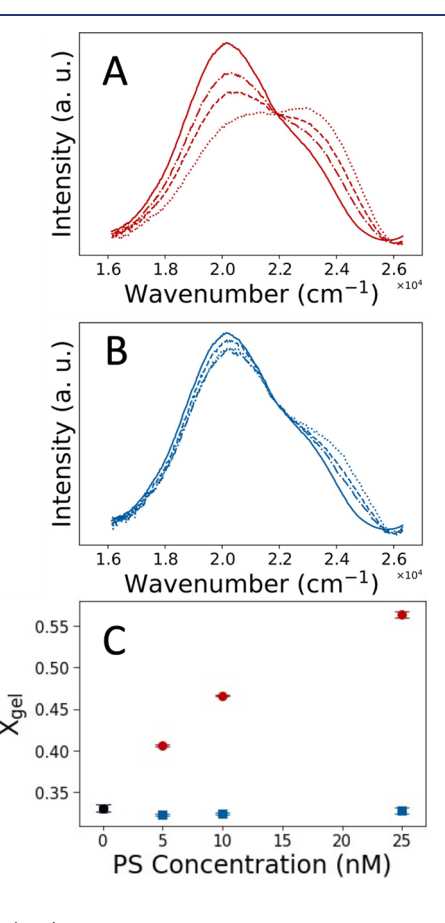


Figure 3. . (A,B) Scatter-subtracted fluorescence spectra of POPC liposomes exposed to (A) PS(-) NPs and (B) PS(+) NPs; line style is according to the PS(-) concentration: 0 nM (-), 5 nM (-), 10 nM (--), and 25 nM (-). (C) $X_{\rm gel}$ calculated as a function of PS NPs concentration: PS(-) NPs red circles, PS(+) NPs blue squares. Error bars represent one standard deviation.

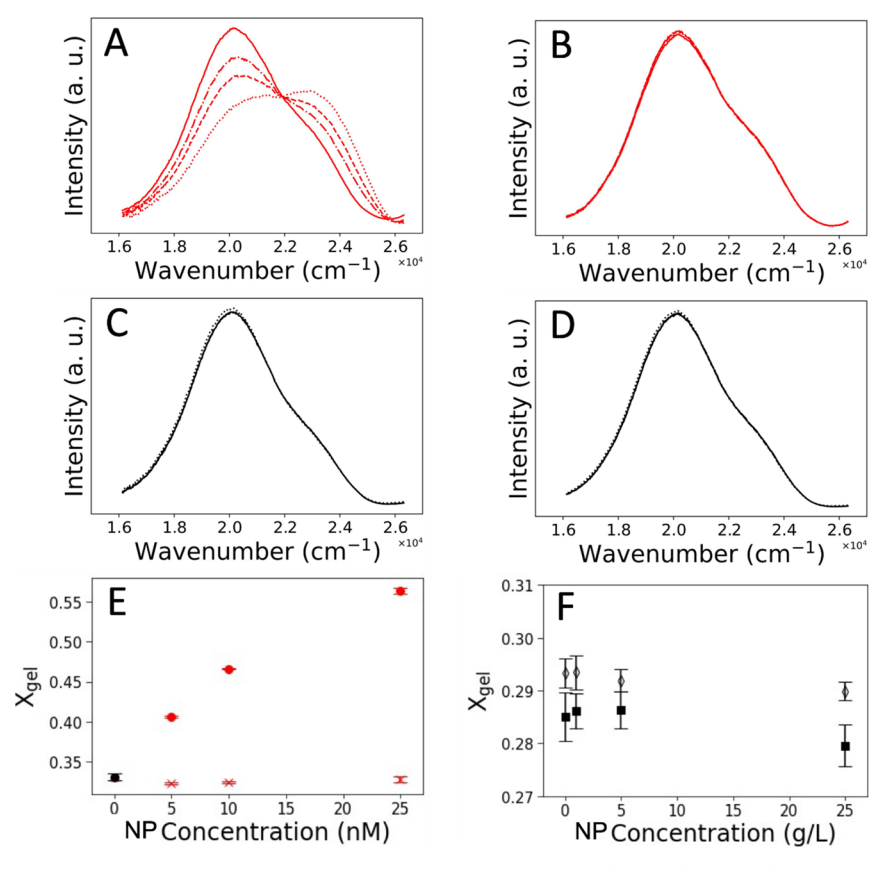


Figure 4. .(A–D) Scatter-subtracted fluorescence spectra of POPC liposomes exposed to (A) PS(–) NPs, (B) PhG NPs, (C) LCO, and (D) NMC nanosheets; line style is according to the PS(–) NPs concentration: 0 nM (—), 5 nM (—·), 10 nM (—·-), and 25 nM (····) for (A,B) and 0 g/L (—), 5 g/L (—·), 10 g/L (—·-), and 25 g/L (····) for (C,D). (E–F) X_{gel} calculated as a function of NP concentration: (E) PS(–) NPs red circles, PhG NPs red ×; (F) LCO nanosheets open triangles, NMC nanosheets black squares. Error bars represent one standard deviation.

 $X_{\rm gel}$ from PS(+) NPs exposure is the second highest of all the NPs studied in this work ($X_{\rm gel~25~nM}-X_{\rm gel~0~nM}=0.04$) but about one fifth of the increase in $X_{\rm gel}$ from PS(-) NPs ($X_{\rm gel~25~nM}-X_{\rm gel~0~nM}=0.23$).

To understand whether the observed difference is solely related to particle surface charge, we measured fluorescence spectra of laurdan in POPC liposomes exposed to varying concentrations of negatively charged NPs. The averaged scatter-subtracted fluorescence spectra are shown in Figure 4A-E. Of these anionic nanoparticles, PS(-) NPs are the only NPs to produce a significant increase in the gel peak (ca. 22,727 cm⁻¹) relative to the fluid peak (ca. 20,408 cm⁻¹) with increasing NP concentration (Figure 4A). The remaining NPs PhG, ND, LCO, and NMC cause no significant change in the fluorescence, even at higher concentrations (Figure 4B-D). The PS(-) NPs at 25 nM are about 5.3 g/L, and yet LCO and NMC nanosheets at higher mass concentrations (25 g/L) cause no discernable change in the membrane phase. Despite the apparent initial stability in HEPES buffer, ND cause significant visible precipitation at the bottom of the sample, evidenced by a sharp decrease in laurdan fluorescence (omitted from figure), indicating a strong binding between ND NPs and the liposomes. This is further indicated by the inability to separate any liposomes from the mixture with ND via size exclusion chromatography. $X_{\rm gel}$ as a function of NP concentration is plotted for PS(-) and PhG NPs in Figure 4E and for LCO and NMC nanosheets in Figure 4F. Due to the precipitation of liposomes by ND, the fluorescence of NDexposed samples could not be deconvoluted into lognormal peaks and analyzed for $X_{\rm gel}$. Again, the only NP with any clear phase effect is PS(-), despite the similar surface charge for all the NPs in Figure 4. The NP core composition and morphology have a significant impact on whether NPs induce a membrane phase change. LCO and NMC nanosheets have large smooth planes in the xy direction, which cannot reach the laurdan molecules which are embedded in the liposomes to induce any change. PhG has hydrophilic branched starches, which have no obvious interaction mechanism: the inert starch would not significantly interact with the head groups on the surface, nor would it interact with the lipid bilayer, which is highly hydrophobic.

It is possible that the strong interactions of PS(-) NPs with zwitterionic lipids compared to the other core materials might be attributed to the hydrophobic nature of PS NPs. Membrane interactions with hydrophobic polymers have been observed previously in lipid bilayer simulations reported by Rossi et al., who found that small PS NPs (10-100 mers) were able to fully penetrate the bilayer within microseconds of reaching the bilayer surface and that this process occurred in part through disaggregation of the polymer chains as we observe in our present simulations.⁵⁰ The same group demonstrated that 7 nm polyethylene, polypropylene, and polystyrene NPs are able to penetrate POPC membranes. 51 Lastly, that group conducted a study that incorporated MD simulations, DSC measurements, as well as both small and wide-angle X-ray scattering (SAXS and WAXS) experiments that demonstrated that PS chains (without cross-links) hindered ordered phase formation by making the membrane more fluid. 52 Thus, as

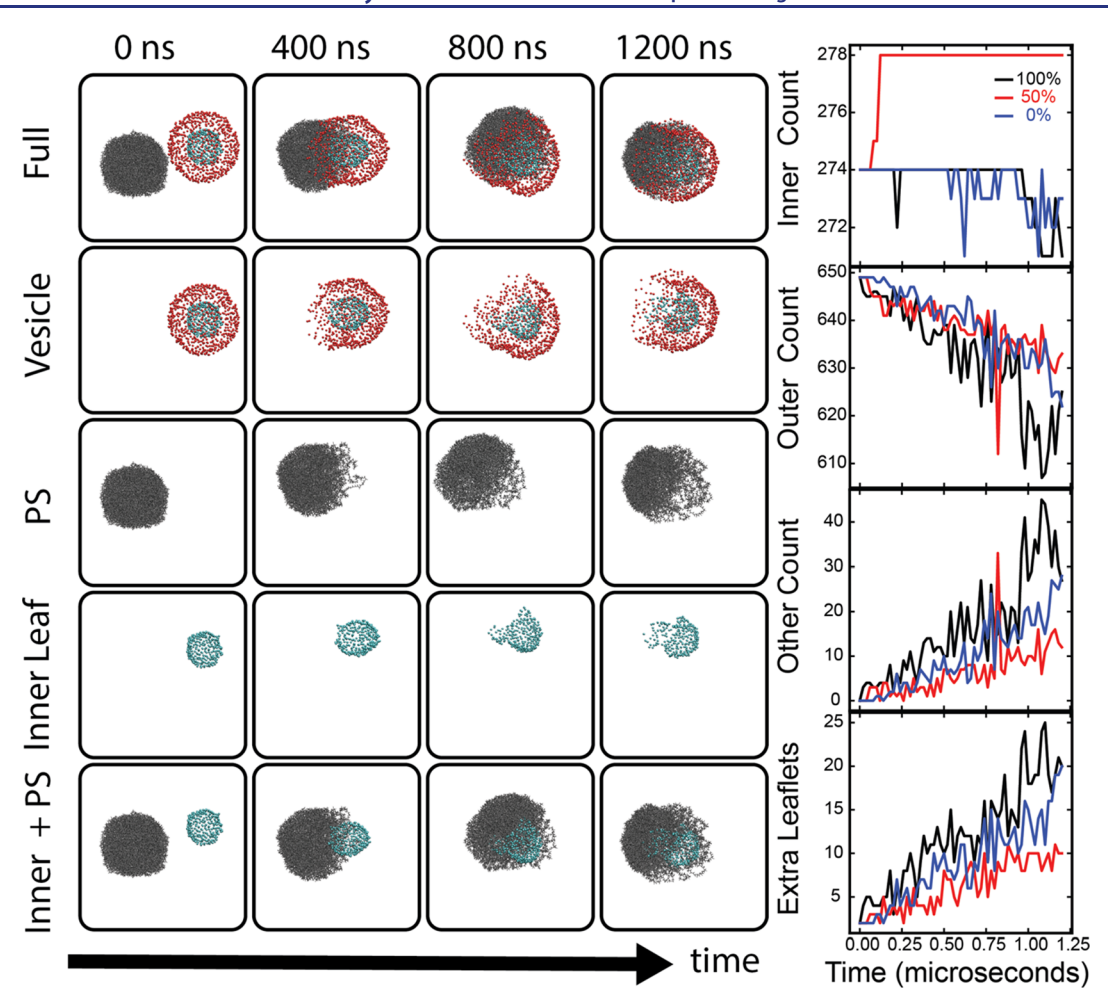


Figure 5. . (A) Timelapse of POPC + PS NP simulation over the course of the 1.2 μ s simulation. For POPC, a single bead per head group is shown colored by whether it is identified in the inner leaflet (teal) or outer leaflet (red) at 0 ns, the PS NP is shown in gray. From top panels to bottom panels, views are presented for the full system, the full liposome, PS NP, the inner leaflet of the liposome, and just the inner leaflet + PS NP; (B) Top 3 Panels: Counts of lipids located in the inner, outer, and other leaflets, respectively. Bottom panel: total number of other leaflets found. Results are shown for the 100, 50, and 0% protonated simulations in black, red, and blue, respectively.

PS(-) NPs are the only NPs in our study which have had any impact on liposome X_{gel} , it is of interest to understand the molecular-level features that drive this effect.

Coarse-Grained Simulations Suggest That Polystyrene Significantly Perturbs the Membrane. To better understand the interactions between PS(-) NPs and phospholipid membranes, we have carried out coarse-grained MD simulations of a PS(-) NP interacting with a pure POPC liposome. Over the course of these simulations, we observed that PS NPs penetrate the outer leaflet of the POPC liposome regardless of protonation state of the nanoparticle. This penetration, illustrated in Figure 5a, is driven by part of the PS chain penetrating the outer leaflet of the liposome. Though PS monomers with carboxyl groups favorably interact with the lipid head groups, the vast majority of PS monomers have favorable interactions with the hydrophobic lipid tails. Thus, once the initial penetration occurs, these interactions draw the polystyrene chains further into the hydrophobic region. By 1200 ns, the chains have nearly fully encased the inner leaflet of the liposome.

Throughout the penetration process, we observe that the inner leaflet of the liposome is deformed but not penetrated by the PS(-) NPs in the timescale of our simulations. In Figure 5A, we have used the LeafletFinder algorithm from the

MDAnalysis software package to color the lipid head groups based on whether they were identified as being part of the inner or outer leaflets at the beginning of the calculation.^{39,53} Aside from some small initial disruption after the initial penetration (as seen in the 0 ns frame), it is clear that the inner leaflet is deformed but remains generally intact over the course of the simulation. To track this, in the top two panels of Figure 5B, we include plots of the counts of lipids in the inner and outer leaflets as functions of simulation time. For all three PS protonation states considered, we see that the inner leaflet count remains remarkably constant indicating that this leaflet remains relatively intact. This is not the case for the outer leaflet, for which we see a significant depletion of lipids for all three simulations. In the third and fourth panels of Figure 5B, we find that these depleted "other" lipids form small clusters of 1-3 lipids, hereafter referred to as "extra" leaflets. These extra leaflet lipids experience significantly different environments than lipids in the liposome, with their tails nearly fully embedded within the polymer. While the number of extra leaflets is similar between the three protonation states, the rate of lipids entering these leaflets is significantly higher for the protonated polymer than the other two cases. If we view this process as an approximate measure of liposome penetration, this indicates that unprotonated carboxyl interactions with

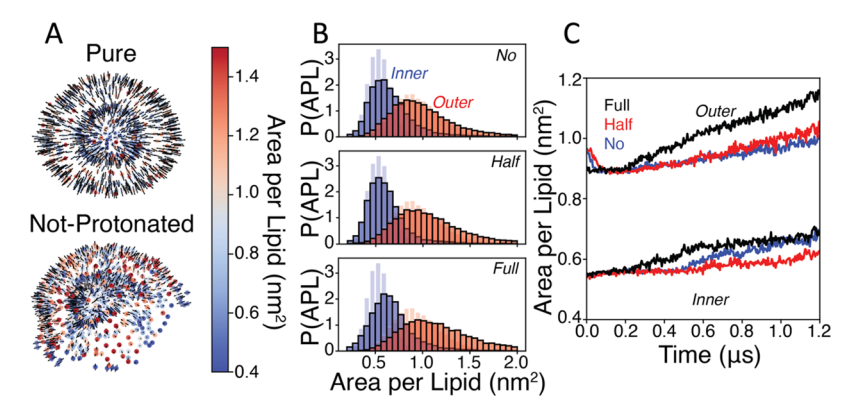


Figure 6. . (A) 3D plots of the lipid head groups colored by the area per lipid for the pure POPC liposome and the half-protonated liposome at the end of their respective simulations. Normal vectors are shown as black arrows. Black arrows without colored circles indicate that the lipid had an unbounded Voronoi cell. (B) Histograms of the area per lipid of the inner (red) and outer (blue) leaflets are shown for each protonation state. Histograms from the pure liposome are included without outlines in the background for reference. (C) Average area per lipids are shown as a function of time for the fully protonated, half-protonated, and unprotonated PS simulations in black, red, and blue, respectively. The top three lines are the outer leaflet, and the bottom three lines are the inner leaflet.

ı

lipid head groups compete to an extent with the polystyrene interaction with the hydrophobic tails.

Importantly, our simulations indicate that the presence of PS(-) NPs leads to significant changes in the local lipid environment of the liposome and thus is expected to significantly modify the environment of laurdan molecules located within the membrane. While typically laurdan has been interpreted in terms of the fluid/gel transition, it is important to note that laurdan reports on the local hydration environment (and its ability to reorient to stabilize the excited state) of the fluorescent probe. Our present hypothesis is that polystyrene dissolved into the hydrophobic region makes this region more hydrophobic by filling in the gaps between lipids with hydrophobic PS chains that force water away from laurdan leading to a more gel-like signal. It should be noted that this manner of penetration is also observed for a membrane in a bilayer configuration (ESI, Figure S8) and thus is unlikely to be caused by the high curvature of the simulated liposomes.

We have additionally calculated the local area per lipid as described in the Materials and Methods section and have included results from this analysis in Figure 6. Figure 6A includes a site-specific view of the lipid packing in both leaflets for the pure liposome and the liposome interacting with the half-protonated PS NP. Interestingly, we see a shift in the outer leaflet to deeper colors of red, indicating that the outer leaflet lipids are becoming less densely packed. In Figure 6B, we include histograms of the area per lipid for both the inner and outer leaflets for each of the protonation states and compare them to the pure liposome. Importantly, we find that the distributions of the inner and outer leaflets both widen and shift to higher areas per lipid. Lastly, in Figure 6C, we include the time dependence of the average area per lipid for each protonation state and leaflet. Our results demonstrate that aside from an initial compression in the outer leaflet as the PS NP first penetrates its head groups, the average area per lipid of both leaflets increases significantly due to the presence of PS in the hydrophobic region of the membrane. Importantly, we have repeated these simulations with DOPC lipids and observed similar behavior (demonstrated in the Supporting Information, Figures S5 and S6). These results indicate that the lipids are not transforming into a pure gel phase; however, they do not rule out that PS NPs may have other effects on the

membrane that would influence the laurdan signal. As laurdan primarily reports on nearby water content, it is possible that PS NPs are forcing water molecules away from laurdan by filling in the gaps opened by the increased area per lipid with PS chains. Furthermore, previously observed PS-induced liposome shrinkage, which had been hypothesized to be due to lipid phase transition, is now explained by our observations of the loss of lipids in the outer leaflet. Future atomistic studies that explicitly include laurdan will be needed to fully deconvolute these processes.

SUMMARY AND CONCLUSIONS

In this study, we investigated the effect of NPs on liposomes using a combination of laurdan fluorescence spectroscopy and coarse-grained MD simulations. The effect of this exposure on the fluorescence spectra was quantified using a novel lognormal deconvolution approach, which we demonstrated was able to yield similar $X_{\rm gel}$ values when liposomes are exposed to PS(-) NPs of increasing concentrations to intensity-based approaches. Likewise, we demonstrated that this approach was able to differentiate between PS(-) NPs concentrations of 0 and 0.5 nM, whereas traditional intensitybased methods detected no significant difference in this concentration range. We demonstrated using this approach that of a wide-variety of NPs (with varied surface charges and core compositions), only PS(-) NPs induced significant changes in the fluorescence spectra. Though negatively charged NPs have largely been understood to have reduced interactions with negatively charged and zwitterionic membranes compared to positively charged NPs, our study shows that when in close proximity, PS(-) NPs strongly interact with zwitterionic lipids by dissolving into the hydrophobic region between leaflets.

Given the uniqueness of the strong interactions between PS(-) NPs and zwitterionic liposomes, we conducted coarsegrained MD simulations to gain a molecular-level understanding of these interactions. These simulations indicate that this effect is driven by penetration of the liposome by chains that unravel from the polymer. Unlike cationic NPs which have only induced moderate amounts of lipid restructuring, our simulations demonstrate that anionic PS(-) NPs interact preferentially with the lipid hydrophobic region, leading to a significant disruption of the structure of the outer leaflet that

could lead to decrease of hydration around laurdan; the latter is expected to lead to the observation of gel-like signals. Likewise, our simulations appear to suggest that a traditional gel phase is not formed, and instead, the area between lipids is expanded by polystyrene. We believe that this expansion increases the hydrophobicity of the membrane, which restricts the ability of water molecules in the membrane to reorganize around the laurdan excited state, leading to the observed blue shift in the fluorescence. Future work will use atomistic and mixed-quantum classical simulations to explore this problem in further detail.

The extensive list of NP types relevant to studies on the impact of NPs on membrane phase change has not been exhausted. In particular, the many secondary nanoplastics (degradation products) of commercial plastics made from polymers such as polyethylene (PE), polypropylene (PP), poly(vinyl chloride) (PVC), polyamides (nylon), polyurethane (PU), and poly(ethylene terephthalate) (PET), and others have not been studied. The primary plastic investigated in studies on the biological impact of NPs. The other nanoplastics, which are commonly negatively charged on the surface, also cause membrane phase change, further studies of biological and environmental impacts of these other types of nanoplastics are warranted. Society is becoming more aware of the dangers of plastics, but the effects of nanoplastics resulting from degradation of these plastics are still largely unknown.

ASSOCIATED CONTENT

Supporting Information

The Supporting Information is available free of charge at https://pubs.acs.org/doi/10.1021/jacs.2c13403.

Characterization of liposomes and nanoparticles, 4PL fitting, lognormal deconvolution parameters and equations, and limits of detection (PDF)

AUTHOR INFORMATION

Corresponding Authors

Qiang Cui — Department of Chemistry, Boston University, Boston, Massachusetts 02215, United States; oorcid.org/ 0000-0001-6214-5211; Email: qiangcui@bu.edu

Zeev Rosenzweig — Department of Chemistry and Biochemistry, University of Maryland Baltimore County, Baltimore, Maryland 21250, United States; oorcid.org/ 0000-0001-6098-3932; Email: zrosenzw@umbc.edu

Authors

Laura A. Kesner – Department of Chemistry and Biochemistry, University of Maryland Baltimore County, Baltimore, Maryland 21250, United States

Zeke A. Piskulich – Department of Chemistry, Boston University, Boston, Massachusetts 02215, United States; orcid.org/0000-0003-0304-305X

Complete contact information is available at: https://pubs.acs.org/10.1021/jacs.2c13403

Author Contributions

L.A.K. and Z.A.P. contributed equally to this manuscript and Q.C. and Z.R. are designated as corresponding authors.

Notes

The authors declare no competing financial interest.

ACKNOWLEDGMENTS

This work is supported by the National Science Foundation under Grant No. CHE-2001611, the NSF Center for Sustainable Nanotechnology (CSN). The CSN is part of the Centers for Chemical Innovation Program. This work used the Extreme Science and Engineering Discovery Environment (XSEDE), which is supported by NSF grant number ACI-1548562. XSEDE simulations were performed on Expanse at the San Diego Supercomputing Center (SDSC) through allocation TG-MCB110014. It should be noted that following completion of the present simulations, XSEDE has been replaced by NSF ACCESS. The authors are also pleased to acknowledge that a portion of the computational work reported on in this paper was performed on the Shared Computing Cluster, which is administered by Boston University's Research Computing Services.

REFERENCES

- (1) Maurer-Jones, M. A.; Gunsolus, I. L.; Murphy, C. J.; Haynes, C. L. Toxicity of Engineered Nanoparticles in the Environment. *Anal. Chem.* **2013**, *85*, 3036–3049.
- (2) Zhang, X.; Pandiakumar, A. K.; Hamers, R. J.; Murphy, C. J. Quantification of Lipid Corona Formation on Colloidal Nanoparticles from Lipid Vesicles. *Anal. Chem.* **2018**, *90*, 14387–14394.
- (3) Wei, X.; Yu, J.; Ding, L.; Hu, J.; Jiang, W. Effect of Oxide Nanoparticles on the Morphology and Fluidity of Phospholipid Membranes and the Role of Hydrogen Bonds. *J. Environ. Sci.* **2017**, 57, 221–230.
- (4) Nel, A. E.; Mädler, L.; Velegol, D.; Xia, T.; Hoek, E. M. V.; Somasundaran, P.; Klaessig, F.; Castranova, V.; Thompson, M. Understanding Biophysicochemical Interactions at the Nano–Bio Interface. *Nat. Mater.* **2009**, *8*, 543–557.
- (5) Williams, D. N.; Pramanik, S.; Brown, R. P.; Zhi, B.; McIntire, E.; Hudson-Smith, N. V.; Haynes, C. L.; Rosenzweig, Z. Adverse Interactions of Luminescent Semiconductor Quantum Dots with Liposomes and *Shewanella Oneidensis*. ACS Appl. Nano Mater. 2018, 1, 4788–4800.
- (6) Zheng, Z.; Saar, J.; Zhi, B.; Qiu, T. A.; Gallagher, M. J.; Fairbrother, D. H.; Haynes, C. L.; Lienkamp, K.; Rosenzweig, Z. Structure—Property Relationships of Amine-Rich and Membrane-Disruptive Poly(Oxonorbornene)-Coated Gold Nanoparticles. *Langmuir* 2018, 34, 4614–4625.
- (7) Wang, S.; Hunter, L. A.; Arslan, Z.; Wilkerson, M. G.; Wickliffe, J. K. Chronic Exposure to Nanosized, Anatase Titanium Dioxide Is Not Cyto- or Genotoxic to Chinese Hamster Ovary Cells. *Environ. Mol. Mutagen.* **2011**, *52*, 614–622.
- (8) Adam, N.; Leroux, F.; Knapen, D.; Bals, S.; Blust, R. The Uptake and Elimination of ZnO and CuO Nanoparticles in Daphnia Magna under Chronic Exposure Scenarios. *Water Res.* **2015**, *68*, 249–261.
- (9) Wang, B.; Zhang, L.; Bae, S. C.; Granick, S. Nanoparticle-Induced Surface Reconstruction of Phospholipid Membranes. *Proc. Natl. Acad. Sci. U. S. A.* **2008**, *105*, 18171–18175.
- (10) Kanwa, N.; Patnaik, A.; De, S. K.; Ahamed, M.; Chakraborty, A. Effect of Surface Ligand and Temperature on Lipid Vesicle—Gold Nanoparticle Interaction: A Spectroscopic Investigation. *Langmuir* **2019**, *35*, 1008–1020.
- (11) Amaro, M.; Reina, F.; Hof, M.; Eggeling, C.; Sezgin, E. Laurdan and Di-4-ANEPPDHQ Probe Different Properties of the Membrane. *J. Phys. D: Appl. Phys.* **2017**, *50*, 134004.
- (12) Dodes Traian, M. M.; Flecha, F. L. G.; Levi, V. Imaging Lipid Lateral Organization in Membranes with C-Laurdan in a Confocal Microscope. *J. Lipid Res.* **2012**, *53*, 609–616.
- (13) Bhat, A.; Edwards, L. W.; Fu, X.; Badman, D. L.; Huo, S.; Jin, A. J.; Lu, Q. Effects of Gold Nanoparticles on Lipid Packing and Membrane Pore Formation. *Appl. Phys. Lett.* **2016**, *109*, 263106.
- (14) Han, J.; Suga, K.; Hayashi, K.; Okamoto, Y.; Umakoshi, H. Multi-Level Characterization of the Membrane Properties of

- Resveratrol-Incorporated Liposomes. J. Phys. Chem. B 2017, 121, 4091–4098.
- (15) Vequi-Suplicy, C. C.; Coutinho, K.; Lamy, M. T. New Insights on the Fluorescent Emission Spectra of Prodan and Laurdan. *J. Fluoresc.* **2015**, *25*, 621–629.
- (16) Bacalum, M.; Zorilă, B.; Radu, M. Fluorescence Spectra Decomposition by Asymmetric Functions: Laurdan Spectrum Revisited. *Anal. Biochem.* **2013**, 440, 123–129.
- (17) Kozyra, K. A.; Heldt, J. R.; Gondek, G.; Kwiek, P.; Heldt, J. Influence of DPPC Liposome Concentration on the Fluorescence Properties of PRODAN and LAURDAN. Z. Naturfors. Sect. A—J. Phys. Sci. 2004, 59a, 809—818.
- (18) Umbsaar, J.; Kerek, E.; Prenner, E. J. Cobalt and Nickel Affect the Fluidity of Negatively-Charged Biomimetic Membranes. *Chem. Phys. Lipids* **2018**, *210*, 28–37.
- (19) Parasassi, T.; Krasnowska, E. K.; Bagatolli, L.; Gratton, E. Laurdan and Prodan as Polarity-Sensitive Fluorescent Membrane Probes. *J. Fluoresc.* **1998**, *8*, 365–373.
- (20) Lúcio, A. D.; Vequi-Suplicy, C. C.; Fernandez, R. M.; Lamy, M. T. Laurdan Spectrum Decomposition as a Tool for the Analysis of Surface Bilayer Structure and Polarity: A Study with DMPG, Peptides and Cholesterol. *J. Fluoresc.* **2010**, *20*, 473–482.
- (21) Siano, D. B.; Metzler, D. E. Band Shapes of the Electronic Spectra of Complex Molecules. *J. Chem. Phys.* **1969**, *51*, 1856–1861.
- (22) Burstein, E. A.; Emelyanenko, V. I. Log-Normal Description of Fluorescence Spectra of Organic Fluorophores. *Photochem. Photobiol.* **1996**, *64*, 316–320.
- (23) Bozich, J.; Hang, M.; Hamers, R.; Klaper, R. Core Chemistry Influences the Toxicity of Multicomponent Metal Oxide Nanomaterials, Lithium Nickel Manganese Cobalt Oxide, and Lithium Cobalt Oxide to Daphnia Magna. *Environ. Toxicol. Chem.* **2017**, *36*, 2493–2502.
- (24) Hang, M. N.; Gunsolus, I. L.; Wayland, H.; Melby, E. S.; Mensch, A. C.; Hurley, K. R.; Pedersen, J. A.; Haynes, C. L.; Hamers, R. J. Impact of Nanoscale Lithium Nickel Manganese Cobalt Oxide (NMC) on the Bacterium *Shewanella Oneidensis* MR-1. *Chem. Mater.* 2016, 28, 1092–1100.
- (25) LIPOSOMES: Methods and Protocols; D'Souza, G. G. M., Ed.; HUMANA Press: Boston, 2018 pp 17-22
- (26) Holstein, C. A.; Griffin, M.; Hong, J.; Sampson, P. D. Statistical Method for Determining and Comparing Limits of Detection of Bioassays. *Anal. Chem.* **2015**, *87*, 9795–9801.
- (27) Marrink, S. J.; Risselada, H. J.; Yefimov, S.; Tieleman, D. P.; De Vries, A. H. The MARTINI Force Field: Coarse Grained Model for Biomolecular Simulations. *J. Phys. Chem. B.* **2007**, *111*, 7812–7824.
- (28) Rossi, G.; Monticelli, L.; Puisto, S. R.; Vattulainen, I.; Ala-Nissila, T. Coarse-Graining Polymers with the MARTINI Force-Field: Polystyrene as a Benchmark Case. *Soft Matter* **2011**, *7*, 698–708.
- (29) Jo, S.; Kim, T.; Iyer, V.; Im, W. CHARMM-GUi: A Web-Based Graphical User Interface for CHARMM. *J. Comput. Chem.* **2009**, 29, 1859–1865.
- (30) Qi, Y.; Ingólfsson, H. I.; Cheng, X.; Lee, J.; Marrink, S. J.; Im, W. CHARMM-GUI Martini Maker for Coarse-Grained Simulations with the Martini Force Field. *J. Chem. Theory Comput.* **2015**, *11*, 4486–4494.
- (31) Choi, Y. K.; Park, S.-J.; Park, S.; Kim, S.; Kern, N. R.; Lee, J.; Im, W. CHARMM-GUI Polymer Builder for Modeling and Simulation of Synthetic Polymers. *J. Chem. Theory Comput.* **2021**, 17, 2431–2443.
- (32) Plimpton, S. Fast Parallel Algorithms for Short-Range Molecular Dynamics. *J. Comput. Phys.* **1995**, *117*, 1–19.
- (33) Martyna, G. J.; Tobias, D. J.; Klein, M. L. Constant Pressure Molecular Dynamics Algorithms. *J. Chem. Phys.* **1994**, *101*, 4177–4189.
- (34) Nosé, S. A Unified Formulation of the Constant Temperature Molecular Dynamics Methods. *J. Chem. Phys.* **1984**, *81*, 511–519.
- (35) Hoover, W. G. Canonical Dynamics: Equilibrium Phase-Space Distributions. *Phys. Rev. A* **1985**, *31*, 1695–1697.

- (36) Jewett, A. I.; Stelter, D.; Lambert, J.; Saladi, S. M.; Roscioni, O. M.; Ricci, M.; Autin, L.; Maritan, M.; Bashusqeh, S. M.; Keyes, T.; Dame, R. T.; Shea, J. E.; Jensen, G. J.; Goodsell, D. S. Moltemplate: A Tool for Coarse-Grained Modeling of Complex Biological Matter and Soft Condensed Matter Physics. *J. Mol. Biol.* **2021**, *433*, 166841–166841.
- (37) Humphrey, W.; Dalke, A.; Schulten, K. VMD: Visual Molecular Dynamics. *J. Mol. Graphics* **1996**, *14*, 33–38.
- (38) Buchoux, S. FATSLiM: A Fast and Robust Software to Analyze MD Simulations of Membranes. *Bioinformatics* **2017**, *33*, 133–134.
- (39) Gowers, R.; Linke, M.; Barnoud, J.; Reddy, T.; Melo, M.; Seyler, S.; Domański, J.; Dotson, D.; Buchoux, S.; Kenney, I.; Beckstein, O. MDAnalysis: A Python Package for the Rapid Analysis of Molecular Dynamics Simulations; Proceedings of the Python in Science Conference (SciPy2016); Austin, TX; 2016; pp 98–105, DOI: 10.25080/Majora-629e541a-00e.
- (40) McElhaney, R. N. The Use of Differential Scanning Calorimetry and Differential Thermal Analysis in Studies of Model and Biological Membranes. *Chem. Phys. Lipids* **1982**, *30*, 229–259.
- (41) Leekumjorn, S.; Sum, A. K. Molecular Characterization of Gel and Liquid-Crystalline Structures of Fully Hydrated POPC and POPE Bilayers. *J. Phys. Chem. B* **2007**, *111*, 6026–6033.
- (42) Tukey, J. W. Comparing Individual Means in the Analysis of Variance. *Biometrics* **1949**, *5*, 99.
- (43) Atkins, P. W.; De Paula, J. *Physical Chemistry: Thermodynamics, Structure, and Change,* 10th ed.; W.H. Freeman: New York, 2014, pp 476–482.
- (44) Cooper, G. M. Cell Membranes. In *The Cell: A Molecular Approach*; Sinauer Associates: Sunderland, MA, 2000.
- (45) Zhang, Y.; Dahal, U.; Feng, Z. V.; Rosenzweig, Z.; Cui, Q.; Hamers, R. J. Influence of Surface Ligand Molecular Structure on Phospholipid Membrane Disruption by Cationic Nanoparticles. *Langmuir* **2021**, *37*, 7600–7610.
- (46) Zhang, Y.; Hudson-Smith, N. V.; Frand, S. D.; Cahill, M. S.; Davis, L. S.; Feng, Z. V.; Haynes, C. L.; Hamers, R. J. Influence of the Spatial Distribution of Cationic Functional Groups at Nanoparticle Surfaces on Bacterial Viability and Membrane Interactions. *J. Am. Chem. Soc.* **2020**, *142*, 10814–10823.
- (47) Atukorale, P. U.; Guven, Z. P.; Bekdemir, A.; Carney, R. P.; Van Lehn, R. C.; Yun, D. S.; Jacob Silva, P. H.; Demurtas, D.; Yang, Y.-S.; Alexander-Katz, A.; Stellacci, F.; Irvine, D. J. Structure—Property Relationships of Amphiphilic Nanoparticles That Penetrate or Fuse Lipid Membranes. *Bioconjugate Chem.* **2018**, 29, 1131–1140.
- (48) Canepa, E.; Salassi, S.; de Marco, A. L.; Lambruschini, C.; Odino, D.; Bochicchio, D.; Canepa, F.; Canale, C.; Dante, S.; Brescia, R.; Stellacci, F.; Rossi, G.; Relini, A. Amphiphilic Gold Nanoparticles Perturb Phase Separation in Multidomain Lipid Membranes. *Nanoscale* **2020**, *12*, 19746–19759.
- (49) Evans, K. O.; Laszlo, J. A.; Compton, D. L. Carboxyl-Terminated PAMAM Dendrimer Interaction with 1-Palmitoyl-2-Oleoyl Phosphocholine Bilayers. *Biochim. Biophys. Acta, Biomembr.* **2014**, *1838*, 445–455.
- (50) Rossi, G.; Barnoud, J.; Monticelli, L. Polystyrene Nanoparticles Perturb Lipid Membranes. J. Phys. Chem. Lett. 2014, 5, 241–246.
- (51) Bochicchio, D.; Panizon, E.; Monticelli, L.; Rossi, G. Interaction of Hydrophobic Polymers with Model Lipid Bilayers. *Sci. Rep.* **2017**, *7*, 1–9.
- (52) Bochicchio, D.; Cantu, L.; Vittoria, M.; Palchetti, L.; Natali, F.; Monticelli, L.; Rossi, G.; Del, E. Polystyrene Perturbs the Structure, Dynamics, and Mechanical Properties of DPPC Membranes: An Experimental and Computational Study. *J. Colloid Interface Sci.* **2022**, 605, 110–119.
- (53) Michaud-Agrawal, N.; Denning, E. J.; Woolf, T. B.; Beckstein, O. MDAnalysis: A Toolkit for the Analysis of Molecular Dynamics Simulations. *J. Comput. Chem.* **2011**, *32*, 2319–2327.
- (54) Krueger, M. C.; Harms, H.; Schlosser, D. Prospects for Microbiological Solutions to Environmental Pollution with Plastics. *Appl. Microbiol. Biotechnol.* **2015**, *99*, 8857–8874.

- (55) Della Torre, C.; Bergami, E.; Salvati, A.; Faleri, C.; Cirino, P.; Dawson, K. A.; Corsi, I. Accumulation and Embryotoxicity of Polystyrene Nanoparticles at Early Stage of Development of Sea Urchin Embryos *Paracentrotus Lividus*. *Environ*. *Sci. Technol.* **2014**, 48, 12302–12311.
- (56) Lin, W.; Jiang, R.; Hu, S.; Xiao, X.; Wu, J.; Wei, S.; Xiong, Y.; Ouyang, G. Investigating the Toxicities of Different Functionalized Polystyrene Nanoplastics on Daphnia Magna. *Ecotoxicol. Environ. Saf.* **2019**, *180*, 509–516.
- (57) Luan, L.; Wang, X.; Zheng, H.; Liu, L.; Luo, X.; Li, F. Differential Toxicity of Functionalized Polystyrene Microplastics to Clams (Meretrix Meretrix) at Three Key Development Stages of Life History. *Mar. Pollut. Bull.* **2019**, *139*, 346–354.
- (58) Mattsson, K.; Ekvall, M. T.; Hansson, L.-A.; Linse, S.; Malmendal, A.; Cedervall, T. Altered Behavior, Physiology, and Metabolism in Fish Exposed to Polystyrene Nanoparticles. *Environ. Sci. Technol.* **2015**, *49*, 553–561.
- (59) Qu, M.; Kong, Y.; Yuan, Y.; Wang, D. Neuronal Damage Induced by Nanopolystyrene Particles in Nematode *Caenorhabditis Elegans*. Environ. Sci.: Nano **2019**, *6*, 2591–2601.
- (60) Sun, X.; Chen, B.; Li, Q.; Liu, N.; Xia, B.; Zhu, L.; Qu, K. Toxicities of Polystyrene Nano- and Microplastics toward Marine Bacterium Halomonas Alkaliphila. *Sci. Total Environ.* **2018**, *642*, 1378–1385.
- (61) Varó, I.; Perini, A.; Torreblanca, A.; Garcia, Y.; Bergami, E.; Vannuccini, M. L.; Corsi, I. Time-Dependent Effects of Polystyrene Nanoparticles in Brine Shrimp Artemia Franciscana at Physiological, Biochemical and Molecular Levels. *Sci. Total Environ.* **2019**, *675*, 570–580.
- (62) Tallec, K.; Huvet, A.; Di Poi, C.; González-Fernández, C.; Lambert, C.; Petton, B.; Le Goïc, N.; Berchel, M.; Soudant, P.; Paul-Pont, I. Nanoplastics Impaired Oyster Free Living Stages, Gametes and Embryos. *Environ. Pollut.* **2018**, 242, 1226–1235.
- (63) Saavedra, J.; Stoll, S.; Slaveykova, V. I. Influence of Nanoplastic Surface Charge on Eco-Corona Formation, Aggregation and Toxicity to Freshwater Zooplankton. *Environ. Pollut.* **2019**, 252, 715–722.
- (64) Bellingeri, A.; Bergami, E.; Grassi, G.; Faleri, C.; Redondo-Hasselerharm, P.; Koelmans, A. A.; Corsi, I. Combined Effects of Nanoplastics and Copper on the Freshwater Alga Raphidocelis Subcapitata. *Aquat. Toxicol.* **2019**, *210*, 179–187.
- (65) Brandts, I.; Teles, M.; Gonçalves, A. P.; Barreto, A.; Franco-Martinez, L.; Tvarijonaviciute, A.; Martins, M. A.; Soares, A. M. V. M.; Tort, L.; Oliveira, M. Effects of Nanoplastics on Mytilus Galloprovincialis after Individual and Combined Exposure with Carbamazepine. *Sci. Total Environ.* **2018**, *643*, 775–784.
- (66) Wegner, A.; Besseling, E.; Foekema, E. M.; Kamermans, P.; Koelmans, A. A. Effects of Nanopolystyrene on the Feeding Behavior of the Blue Mussel (*Mytilus Edulis L.*). *Environ. Toxicol. Chem.* **2012**, 31, 2490–2497.
- (67) Tiwari, E.; Singh, N.; Khandelwal, N.; Monikh, F. A.; Darbha, G. K. Application of Zn/Al Layered Double Hydroxides for the Removal of Nano-Scale Plastic Debris from Aqueous Systems. *J. Hazard. Mater.* **2020**, 397, No. 122769.
- (68) Towns, J.; Cockerill, T.; Dahan, M.; Foster, I.; Gaither, K.; Grimshaw, A.; Hazlewood, V.; Lathrop, S.; Lifka, D.; Peterson, G. D.; Roskies, R.; Scott, J. R.; Wilkins-Diehr, N. XSEDE: Accelerating Scientific Discovery. *Comput. Sci. Eng.* **2014**, *16*, 62–74.